NeuroImage **10,** 724–737 (1999)
Article ID nimg.1999.0509, available online at http://www.idealibrary.com on IDEAL®

Accurate High-Speed Spatial Normalization Using an Octree Method

Peter V. Kochunov, Jack L. Lancaster, and Peter T. Fox

Research Imaging Center, University of Texas Health Science Center at San Antonio, 7703 Floyd Curl Drive, San Antonio, Texas 78284

Received December 30, 1998

The goal of regional spatial normalization is to remove anatomical differences between individual three-dimensional (3-D) brain images by warping them to match features of a standard brain atlas. Full-resolution volumetric spatial normalization methods use a high-degree-of-freedom coordinate transform, called a deformation field, for this task. Processing to fit features at the limiting resolution of a 3-D MR image volume is computationally intensive, limiting broad use of full-resolution regional spatial normalization. A highly efficient method, designed using an octree decomposition and analysis scheme, is presented to resolve the speed problem while targeting accuracy comparable to current volumetric methods. Translation and scaling capabilities of octree spatial normalization (OSN) were tested using computer models of solid objects (cubes and spheres). Boundary mismatch between transformed and target objects was zero for cubes and less than 1% for spheres. Regional independence of warping was tested using brain models consisting of a homogenous brain volume with one internal homogenous region (lateral ventricle). Boundary mismatch improved with successively smaller octant-level processing and approached levels of less than 1% for the brain and 5% for the lateral ventricle. Five 3-D MR brain images were transformed to a target 3-D brain image to assess boundary matching. Residual boundary mismatch was approximately 4% for the brain and 8% for the lateral ventricle, not as good as with homogeneous brain models, but similar to other results. Total processing time for OSN with a 256^3 brain image (1-mm voxel spacing) was less than 10 min. © 1999 Academic Press

Key Words: **octree; spatial normalization; homology; warping; Jacobian.**

INTRODUCTION

Spatial normalization refers to a class of image processing algorithms that reduces interindividual anatomical variance by matching homologous spatial features of a "source" brain to those of a "target" brain. In many human brain mapping analyses, an anatomical feature template is used instead of a target brain to spatially transform anatomical and functional 3-D data into a common brain (Fox *et al.,* 1985; Collins *et al.,* 1994; Fox, 1995; Friston *et al.,* 1995; Lancaster *et al.,* 1995; Woods, 1996; Toga *et al.,* 1998). The most common target brain space is that developed by Talairach and colleagues (Talairach *et al.,* 1988).

Spatial normalization can be broadly classified as global or regional. Global normalization uses a parametric description of the whole brain (position, orientation, and dimensions) to perform affine transformations, with up to twelve parameters in a 4×4 homogeneous coordinate transform matrix (Foley *et al.,* 1990). In most instances of global normalization, only nine parameters are used (three each for rotation, translation, and scaling), and these must be carefully selected (Fox, 1995; Woods, 1996). Manual global spatial normalization methods require identification of key landmarks, such as the anterior and posterior commissures (AC, PC), to perform appropriate translation, rotation, and scaling (Fox *et al.,* 1985; Minoshima *et al.,* 1993; Lancaster *et al.,* 1995). Automated global spatial normalization methods, matching features such as the brain's convex hull surface, have also been reported (Lancaster *et al.,* 1999; Collins *et al.,* 1994; Roland *et al.,* 1994). While global spatial normalization methods remove global anatomical differences, they cannot correct for smaller regionalized differences. Regional spatial normalization algorithms try to match homologous spatial features at varying scales, some down to the limiting resolution of 3-D MR brain images (Christensen *et al.,* 1994; Collins *et al.,* 1995).

Previously reported methods (Christensen *et al.,* 1994; Collins *et al.,* 1995; Kostelec *et al.,* 1998) require many hours of processing to produce a full-scale deformation field. The primary goal of the OSN design was to reduce the processing time to minutes while maintaining the accuracy of the previous methods. This improvement for OSN was sought by increasing efficiency in the several areas (Table 1).

This report describes the OSN algorithm and tests several key properties of OSN. Tested properties include: continuity correction, global translation and scaling, management of nonhomologous features, and regional warping performance. Most of these properties

1053-8119/99 $30.00

TABLE 1

Description of the OSN's Algorithm Efficiency

Improvement area	Description
Feature extraction	Centroid matching rather than MSE approach by Collins *et al.* (1995)
Continuity correction	Adaptive Gaussian smoothing (see Material and Methods) as opposed to Navier–Stokes or spline interpolations (Kostelec *et al.,* 1998)
Scale control	Octree volume decomposition with rejection of empty processing nodes
Coding features	Exploiting the parallel nature of the OSN's design with multithreaded code

are evaluated using computer modeled source and target 3-D images to insure absolute measurement of performance quality. In addition, promising applications of high-degree-of-freedom spatial normalization are discussed.

MATERIALS AND METHODS

OSN algorithm overview. The 3-D OSN algorithm evolved from earlier modeling in one and two dimensions (Lancaster *et al.,* 1998). As with prior, high-resolution regional normalization methods (Christensen *et al.,* 1994; Collins *et al.,* 1995; Kostelec *et al.,* 1998), OSN computes a deformation field. It does this in a hierarchical, multiscale manner, by subdividing the volume into successive octants. At each stage, local similarity measurements are made and compared between source and target. The similarity measurements are adaptive, thresholded centers of the mass. Prior to advancing to the next octree subdivision: a deformation field that matches all centers of mass, is computed; continuity correction is performed; and deformation field is applied. The octree design, coupled with new processing strategies, provides a significant improvement in processing efficiency over existing methods. Scale control, achieved using 3-D Gaussian filtering and resampling by Collins *et al.* (1995), is much simpler in OSN being a natural feature of the progressive subdivision of the 3-D volume into identical octants. Additionally, void octants outside the brain volume are sequentially removed from the processing list, reducing the processing load by approximately 75%.

The similarity measurement scheme for OSN is efficient and simple, yet powerful. For each octant, the spatial centroid is the feature of interest. It is calculated from the set of voxels with values above or below an adaptive threshold. The adaptive threshold value is the mean value of data within each octant. The x-y-z translation needed to match centroids of transformed-source and target octants is then used to refine the deformation field. Several strategies for calculating the centroid were previously tested, and the thresholded geometrical (unweighted) centroid provided the best performance (Lancaster *et al.,* 1998).

Regional spatial normalization is usually preceded by global spatial normalization, to provide a source image with standard position, orientation, and scaling. The globally normalized starting image establishes a spatial reference frame for reporting results in OSN (processing step 0). The Convex Hull global fitting method was used for global normalization. This algorithm has been validated relative to the 1988 Talairach Atlas space (Lancaster *et al.,* 1999), the space most commonly used for reporting coordinate based findings in brain mapping experiments.

The OSN method requires that 3-D images and deformation arrays be cubic, i.e., same number of voxels for x, y, and z dimensions, and that each dimension (D) be defined as 2^N where N is a positive integer. N is also the number of OSN processing steps. Therefore for a 256^3 array there are eight processing steps (0–7). As processing progresses from step 0 to step 7, its regional/scale nature changes from a single region of size 256^3 to 2,097,152 regions of size 2^3. This hierarchical multiscale processing scheme follows from the natural octree subdivision of space and results in an extremely efficient algorithm for synthesis of a high degree of freedom deformation field.

Continuity correction. The octree algorithm requires independent shifting of image data within octants. This leads to discontinuous regions in the transformed image due of motion perpendicular to (overlapping or tearing) and/or parallel to (shearing) interfaces between neighboring octants (Fig. 1). To avoid discontinuities where the deformation gradient exceeds a limiting value, the deformation field was smoothed using a spatial-domain Gaussian filter (see Appendix 1). The FWHM of the filter was selected to keep the magnitude of the derivative of each component of the deformation gradient ($\Delta D_x/\Delta x$, $\Delta D_y/\Delta y$, $\Delta D_z/\Delta z$) ≤ 0.3, insuring both continuity and 1-to-1 mapping between source and target volumes (Appendix 1). The continuity filtering takes the largest portion of the algorithm run-time. To improve performance, 3-D smoothing was done as three 1-D convolutions along the x, y, and z directions. Further reduction in execution time was achieved by independently adjusting the filter FWHM for each octant boundary, since many boundaries required little or no correction.

To test the continuity correction method, deformations with known levels of discontinuity were applied to a 3-D solid cube. Continuity-corrected deformations were calculated and compared with known values. 3-D surface renderings of the raw and continuity-corrected transformed cubes were made to qualitatively assess performance over the entire surface.

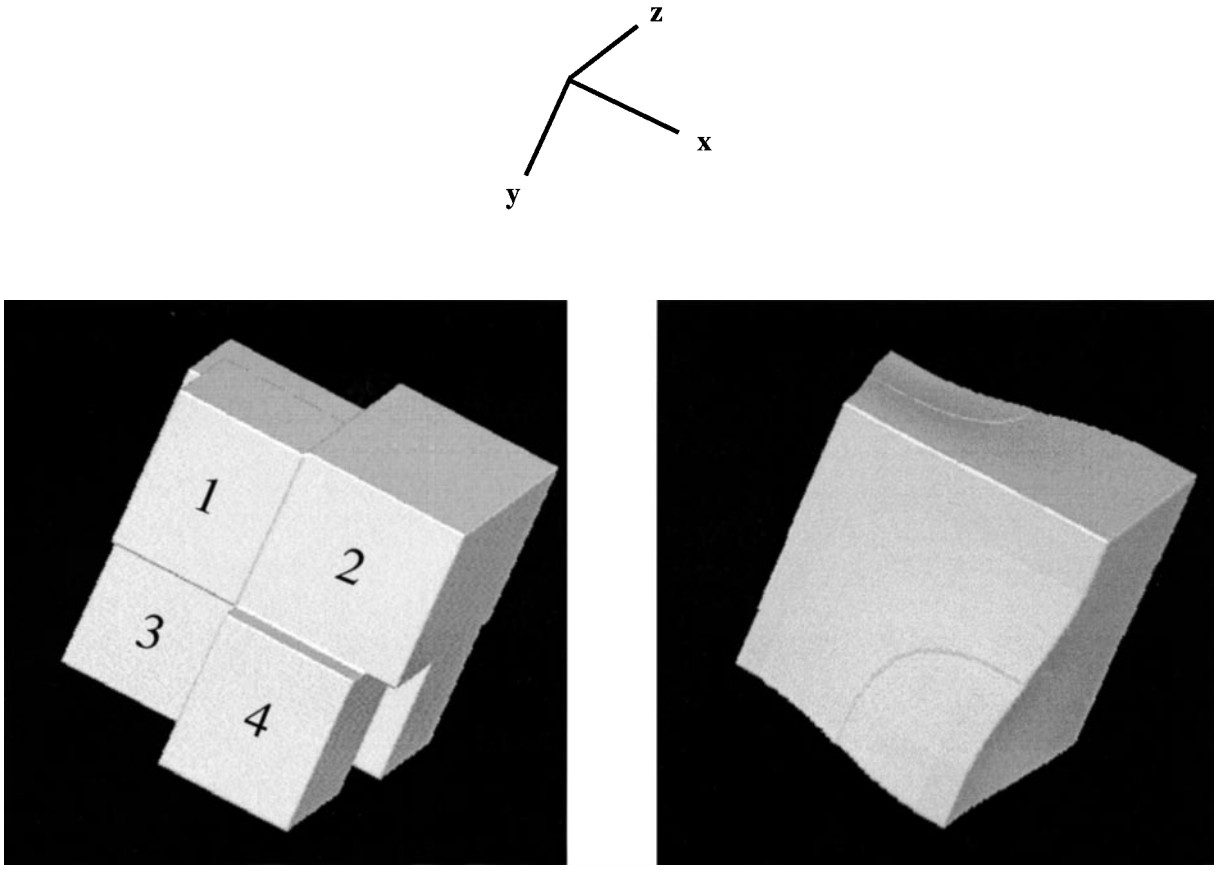

FIG. 1. Computer-rendered views of a solid cube deformed with continuity correction (right) and without continuity correction (left). Examples of shearing (2–4), tearing (4–8), and overlapping (1–2) are seen in the uncorrected data. Octant regions of deformed cube were clipped at the step-1 octant boundaries to help identify them. Octants 5–8 are behind octants 1–4, with 5 behind 1 and so forth.

Global translation and scaling. Global translation and scaling are two important steps in global spatial normalization. Computer models of solid cubes and spheres were created in 256^3 arrays to study translation and scaling with 3-D solid objects. Target and source cubes and spheres of different sizes and locations were modeled. Fit quality was evaluated by comparing OSN transformed source models with target models. Differences between transformed and target objects are only measurable at mismatched boundaries since interior values are identical. To quantify 3-D overlapping, the boundary mismatch (volume of mismatched boundary voxels) was reported as a percentage of the total volume of the target. The boundary mismatch volume was calculated by binary mode subtraction between target and step n-transformed images and saved as a separate image. This method of error reporting provides a quantitative measure of fit quality for any boundary that can be readily identified in target and transformed images. It also provides a means to visualize fit quality for surfaces throughout the image volume. The percentage boundary mismatch as a measure of fit quality is similar to values reported by others (Collins *et al.,* 1995) to evaluate automated segmentation.

To correct for global spatial differences, the center of mass was used for alignment of both cubes and spheres at processing step 0. This removes translation differences therefore translation is not a factor with identical shape geometrical objects; however, the position of the target relative to octant boundaries may have an affect. The roles of source and target images were reversed to evaluate a possible position effect. Nearest-neighbor (N-N) interpolation was used in all tests to ensure accurate boundary definition in transformed images using a single threshold value.

Testing was done to determine if geometric scaling was linear throughout the image volume. The ratio of source-to-target dimensions was used to predict the distance from model centroids to various internal well-defined surfaces, planes for cubes, and shells for spheres. The deformation field was used to calculate a set of points along a source image surface from points along a corresponding target image surface. The mean and standard deviation of the distance from the centroid was calculated for each surface. Seven such surfaces

with distances ranging from 2 to 64 mm were evaluated for the solid model. Overall linearity of global scaling within the solid models was assessed from the slope of a least squares linear regression fit of mean measured vs predicted distances. Differential linearity of global scaling was estimated from the standard deviation of measured distances for each surface.

Matching of nonhomologous regions. OSN can be used to transform a cube to a sphere and vise versa, but since these objects are grossly nonhomologous they give little insight to the nature of this problem in the brain. To test nonhomology in a human brain, a 3-D brain image was modified to introduce several grossly nonhomologous regions. This was accomplished by clipping the brain image posteriorly and inferiorly (Fig. 2, middle). The unmodified brain image was used as the source and the clipped brain image as the target for OSN regional spatial normalization. Since there is no metric to directly assess nonhomology, results were evaluated qualitatively.

Regional performance. Independence of regional warping was tested using two 3-D brain models, each consisting of a homogenous brain region with one internal homogeneous region (lateral ventricle). Source and target brain model images were created from 256^3 T1-weighted MR images by manual segmentation of the brain and lateral ventricle. Manual segmentation followed the brain surface along gyral and shallow sulcal boundaries to isolate the brain from surrounding nonbrain regions. Filling the brain region with a value of 512 and ventricle region with 256 completed the brain model images. Model source and target images were selected from a group of 150 studies as those with the largest subjective difference in brain shape and ventricle size. Source and target brain models were globally spatially normalized using the "convex hull" automated global spatial normalization method (Lancaster *et al.,* 1999). OSN was then used for regional spatial normalization. Boundary mismatch images were calculated at each processing step, and the mismatch for brain and ventricle surfaces was tabulated.

Human brain evaluation. Due to inherent anatomical variability, some degree of nonhomology exists between any two human brains (Talairach *et al.,* 1988; Ono *et al.,* 1990). Failed homology confounds feature matching for regional spatial normalization algorithms and interferes with the selection of landmarks necessary to evaluate fit quality. In fact, fit quality has little meaning when matchable landmarks are not present. A potentially useful goal is to measure fit quality using some subset of matchable landmarks. Regardless, it is important to study the nature of warping of images with varying degrees of nonhomologous features, and this requires a measure of fit quality. Our solution was to measure fit quality by comparing the two well-defined boundaries of major structures, the brain and the lateral ventricle, as was done for regional testing with the brain model data.

Six 3-D, 256^3, T1-weighted MR images of healthy adults were randomly selected from a pool of 150 subjects (18–40 years) for processing. Each image was edited to remove the scalp, skull, and other nonbrain tissues. Surfaces of the brain and the lateral ventricle were carefully defined by removing tissues outside the brain and fluids and tissues inside the ventricle, while leaving the remainder of brain image data intact. The brain stem was removed below the level of cerebellum to better define the inferior margin of the brain. The lateral ventricle was manually segmented and filled with a constant value equal to its mean value. One 3-D brain image was randomly selected as the target. All images were globally spatially normalized using the "convex hull" method to standardize position, dimension, and orientation. Each image was then regionally spatially normalized using OSN. Boundary mismatch images were calculated at each processing step, and the

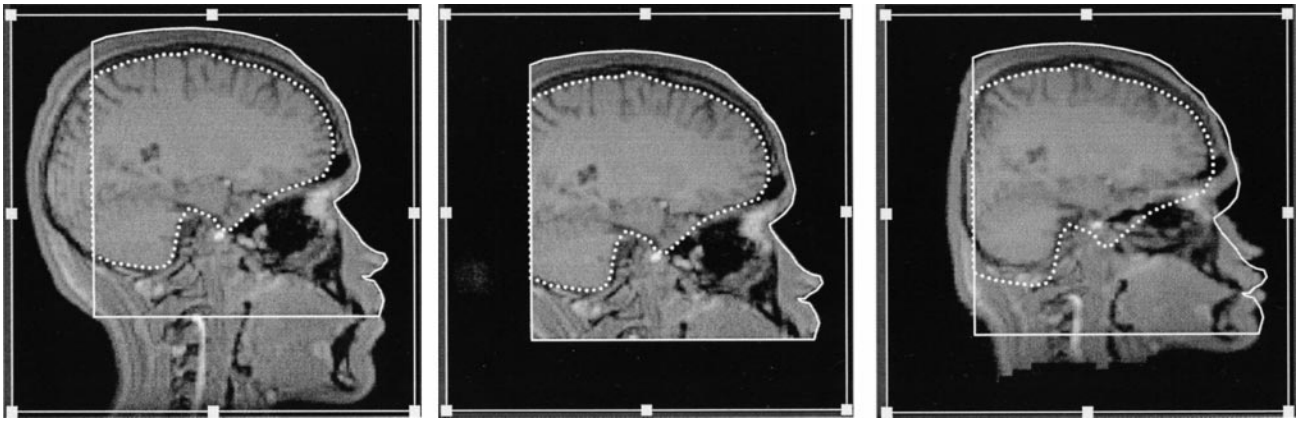

FIG. 2. Matching capability of OSN with grossly nonhomologous source (left) and target (middle) brain images. The transformed image (right) shows how the source brain image is compressed into the target brain region. The head (solid) and brain (broken) outlines provide a visual means to evaluate warping.

mismatch for brain and ventricle surfaces was tabulated.

RESULTS

Continuity correction. Figure 1 (left) shows the result of applying the uncorrected 3-D deformation field to a computer modeled cube. Overlapping regions of the transformed cube were clipped at the step-1 octant boundaries. Object rotation was introduced to provide a better view of the deformed cube. Testing with solid cubes demonstrated that a gradient magnitude ≤ 0.3 for each component of the deformation field provided a continuous deformation.

Profile curves through octant 1 and octant 2 (Fig. 3) illustrate the effects of continuity correction (solid) following planned disruption of the deformation field (broken). The profile curves were drawn along the $+x$ direction so the x deformation represents overlapping (region 1 moved 10 mm in the $+x$ direction, while region 2 was not moved) and the y and z deformations represent shearing. In this example the original cube (not shown) was centered in a 256^3 array and the numbered regions correspond to the octant they occupied at step 0. Only step 1 processing is illustrated. The planned differences in deformation were 10 mm for x, 10 mm for y, and 5 mm for z, and the measured profile curve values showed that these were exactly reproduced.

The continuity-corrected deformation values from the profiles in Fig. 3 were compared with predicted values. The maximum gradients were measured at 0.29 for all three profiles and the target value was 0.3. A 1-D derivative was taken along each profile curve to produce a curve that represented the line spread functions (LSF) of the Gaussian filter (Hasegawa, 1991). The FWHM of the LSF was estimated using nearest neighbor interpolation. For the measured x and y deformations the theoretical FWHM (Appendix 1) was 31.3 mm and the measured value was 35 mm. For the z deformation the theoretical FWHM was 15.7 mm and the measured was 18 mm. By design the extent of the Gaussian filters was clipped at the tails where sum of the filter weights was 95% of the full area. This resulted in an extent of 56 mm for the x and y filters and 28 mm for the z filter. The extent measurements indicate that filtering will alter the interior of deformation octants approximately 5.6 mm from interfaces for each 1 mm of discontinuity.

Global translation and scaling. The boundary mismatch was measured before and after applying OSN to paired cubes and spheres (Table 2). After transformation there were no mismatched voxels observed for the cubes and minimal mismatch for the spheres. The surface of the sphere was harder to fit, and while some surface points transform to exact voxel coordinates, most do not. This leads to larger N-N interpolation errors, but the final boundary mismatch remained

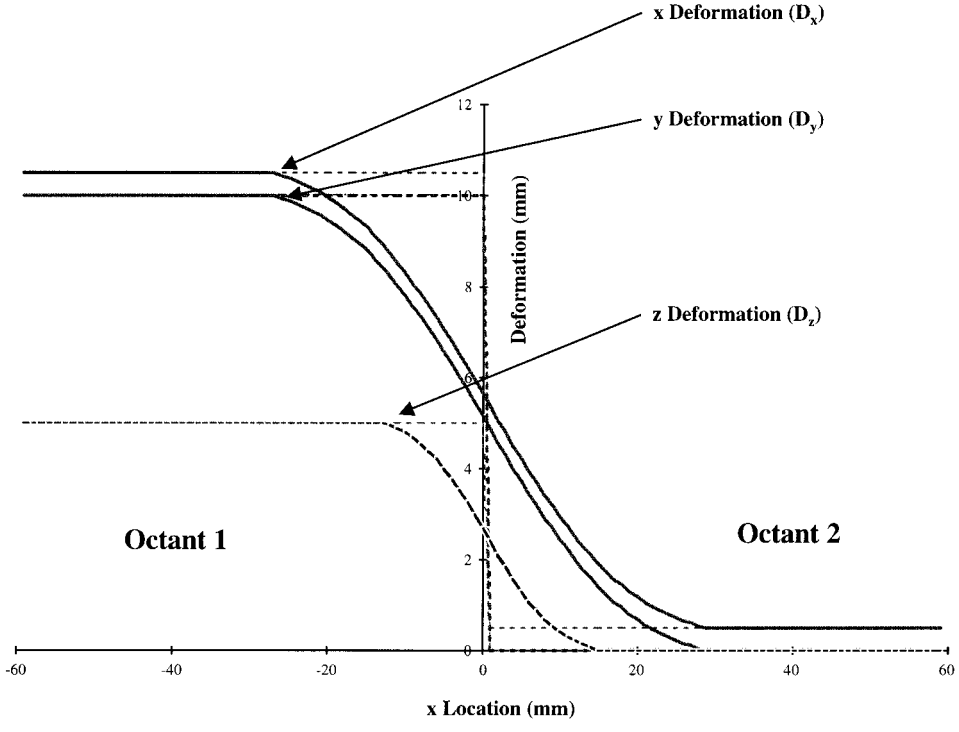

FIG. 3. Profiles curves for x-, y-, and z deformations between regions 1 and 2 of the deformed cube described in the legend of Fig. 1. The raw deformations (broken lines) and continuity corrected deformations (solid lines) show the importance of continuity correction.

TABLE 2

Percent Boundary Mismatch for OSN

Objects	Source size	Target size	Initial mismatch	Final mismatch
Cubes	128	161	100%	0.0%
Spheres	168	128	120%	0.1%

small (0.1%). The position of the target object had little effect on fit quality since the final mismatch figures were nearly identical to those in Table 2, when the source and target objects were swapped. The small residual mismatch shows that centroid matching by OSN can effectively scale simple (cube) and more complex (sphere) geometrical objects.

The stepwise progress of the OSN processing in transforming a sphere from a diameter of 168 to 128 mm was seen to be a successive scaling of the size of the sphere. Minor shape distortions were visible during early processing steps, and a nearly perfect spherical shape was formed by the final step (Fig. 4). This was indicated by the small RMS error in the radial distance from points along the surface of the transformed source sphere to those of the target sphere (0.6 mm). This error is similar to that observed when fitting brain surfaces from the same individual but different image modalities (Lancaster *et al.,* 1999). The mean RMS error was calculated using the XSurfaceFit software (Pelizzari, 1991).

The graph of mean measured vs predicted distance (Fig. 5) within the cube and spherical models demonstrated excellent global linearity of scaling. The linear regression line had a slope within 1% of unity and intercept within 0.4 mm of zero for both models. This was strong evidence that the global scaling properties of the OSN method are correct throughout the solid models. Regional linearity of scaling was also very good, with the mean standard deviation of distance for the seven surfaces tested in the sphere of 0.035 mm. The maximum errors for each surface were generally less than the voxel spacing (1 mm). The average of worst-case errors across all surfaces was 0.79 mm above or 0.68 mm below the predicted distance. These data indicate that OSN can provide accurate and linear scaling across homogeneous areas, even those far from a boundary.

These results support the idea that multiscale centroid shifting with continuity correction is capable of performing a transformation equivalent to a linear global scaling. This is a major achievement since there is little regional information throughout the volume of the homogeneous cubes and spheres.

Matching of nonhomologous regions. The sagittal section images in Fig. 2 illustrate the performance of OSN under conditions of grossly mismatched homology

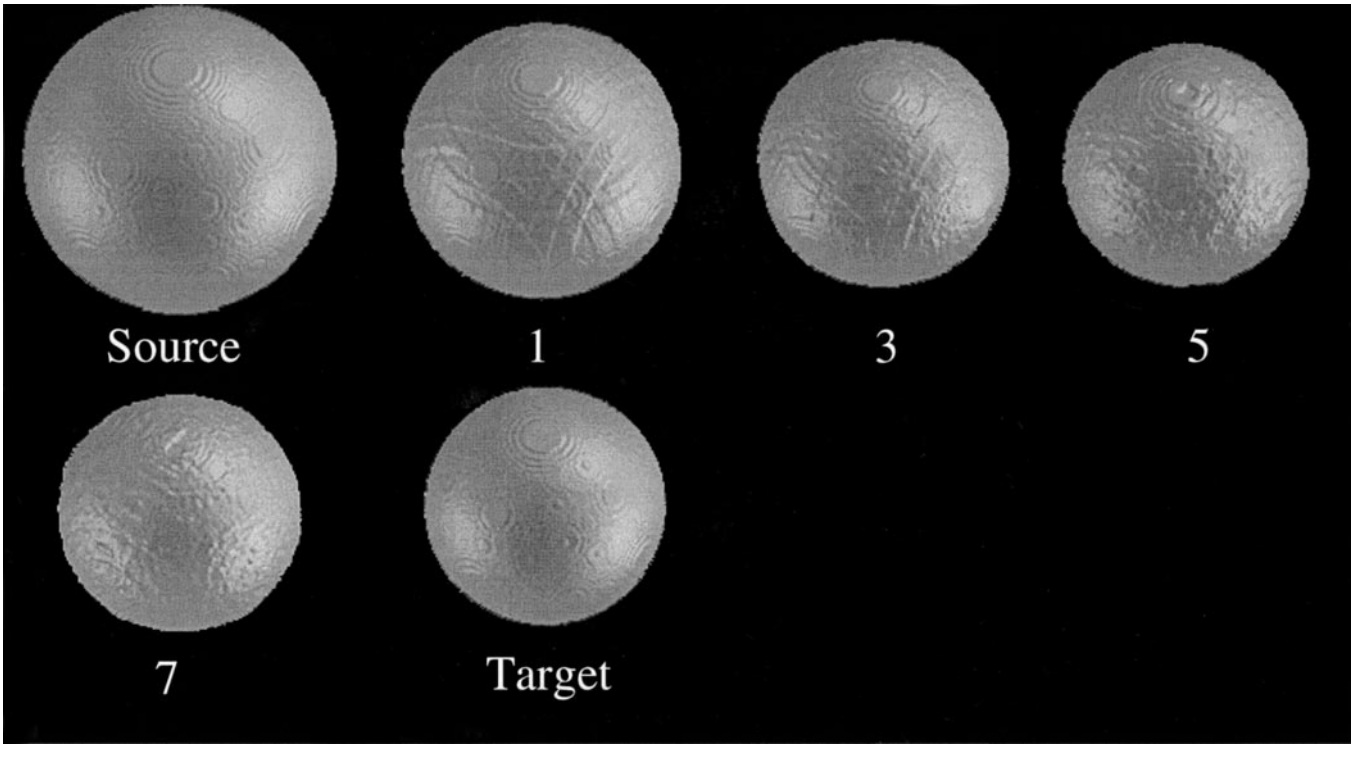

FIG. 4. Source and target spheres with results of steps 1, 3, 5, and 7 of OSN processing.

between source and target brain-like images. The small boxes near the periphery of each image delimit the step-1 octant subdivision of these images. The solid white outline is the target head boundary, and the broken line is the approximate target brain boundary, both traced from the target image (Fig. 2, middle). The mismatch along the inferior and posterior boundaries between source and target images is large (Fig. 2, left). There was no mismatch along the major extent of the superior and anterior boundaries. Inferior and posterior boundary mismatches were greatly reduced following the OSN transformation (Fig. 2, right). OSN transformation resulted in compression of the image volume from the inferior and posterior regions into the target volume. Head and brain boundaries in the upper right quadrant were less affected, but were more affected in the S-I direction than the A-P direction. This was attributed to the fact that a much larger volume of tissue was compressed into the target volume from regions inferior to the target volume than from posterior regions.

While OSN did not perform perfectly in any of the octants, it did perform according to the algorithm's design goals. In particular there are no obvious discontinuities and regions further from the gross feature mismatched regions had a better match. The full volume of the source image was transformed into the approximate volume of the target (distorted) brain. The initial volume difference was 20%, and OSN processing reduced this to less than 5%. This example shows that

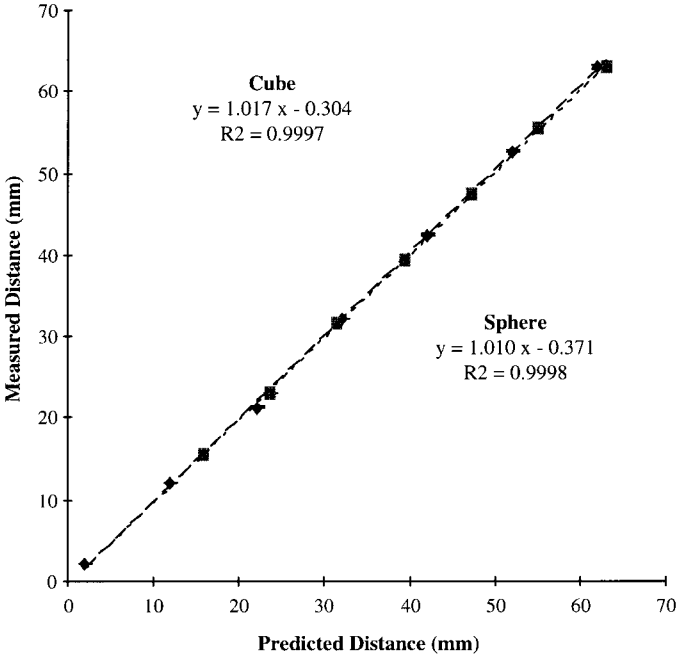

FIG. 5. Measured vs predicted distance inside cube (diamond) and sphere (square) following OSN transformation to match a different size cube and sphere.

FIG. 6. Sagittal view of boundary mismatches for computer modeled brain with lateral ventricle following Convex Hull global spatial normalization (top) and OSN regional spatial normalization (bottom).

the OSN algorithm provides a predictable, stable spatial transformation even when significant feature mismatches are present.

Regional performance. The midsagittal view of mismatched boundaries for the 3D brain model shows significant regional improvement following OSN processing for both the brain and ventricle surfaces (Fig. 6). In fact, most of the mismatched regions for the OSN brain image were of the order of the voxel dimension.

Percentage mismatch of the *brain* boundary for OSN at each processing step decreased monotonically (Fig. 7). The initial percentage mismatch (step 0) is that following global spatial normalization and the final (step 7) is that for full regional spatial normalization. The final mismatch is similar to that achieved by OSN for the computer modeled solid spheres (<1%). The *ventricle* mismatch increased initially, followed by a decreasing trend (Fig. 7). The rise in ventricle mismatch during the first two processing steps is believed to be due to its relatively small size. OSN multiscale processing deals with large-scale features during the early steps of

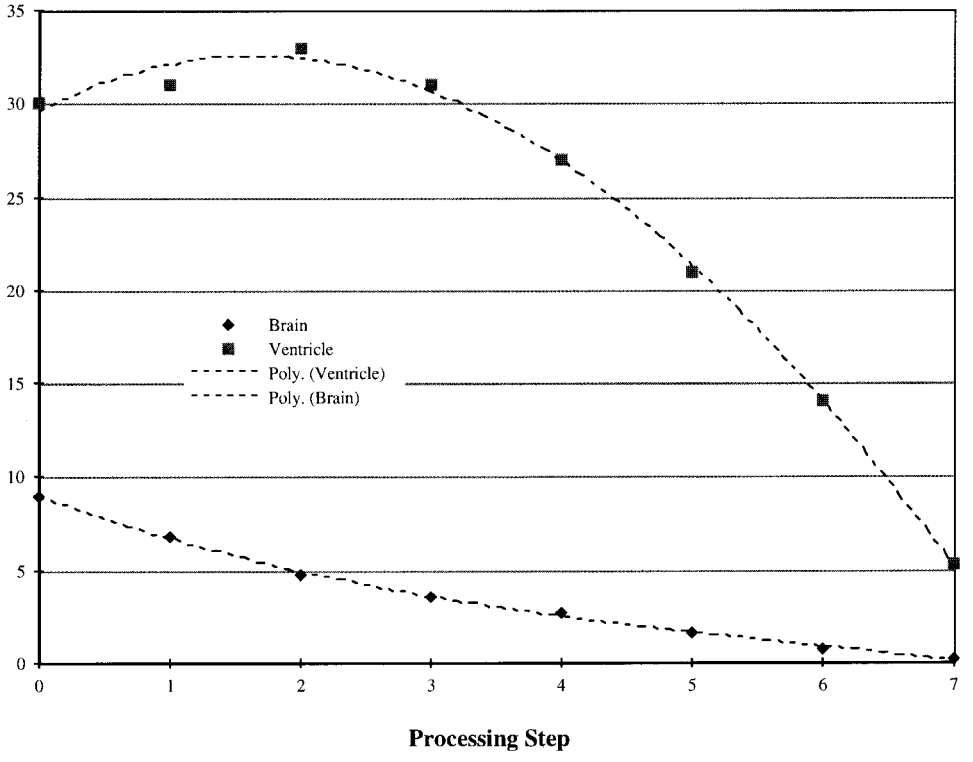

FIG. 7. Percentage boundary mismatch at each step of OSN processing for brain and lateral ventricle for fitting brain models.

regional processing. The boundary mismatch for small-scale features can therefore rise during these out-of-scale processing steps. This rise is compensated later as the regional processing scale decreases. In fact, the slope of the percentage mismatch curve is steeper for the ventricle than for the brain for steps 3–7 (Fig. 8B). The ventricle percentage mismatch following global spatial normalization (5%) is a six-fold reduction from the 30% mismatch following regional spatial normalization, but does not achieve the 1% level seen for the brain surface.

Human brain evaluation. The midsagittal view of one transformed human brain illustrates typical improvement of OSN over global spatial normalization (Fig. 8), for the ventricle and brain boundary, the cerebellum, and the superior temporal lobe. The mean percentage mismatch curves for OSN processing of the five human brain images shows a continual improvement in fit for each successive step for both brain and ventricle (Fig. 9). The rise in percentage mismatch for the ventricle, seen with the homogeneous brain model,

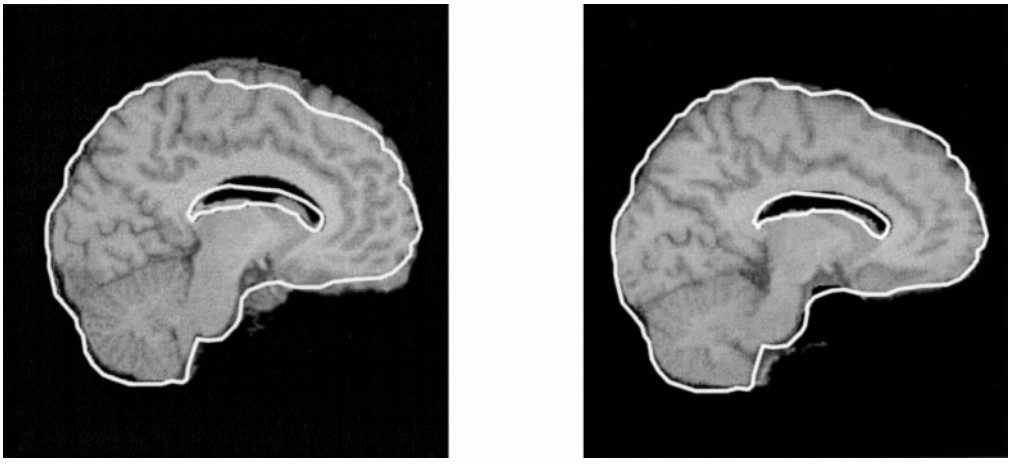

FIG. 8. Sagittal views of human brain following Convex Hull global spatial normalization (left) and OSN regional spatial normalization (right). The outline of the target brain and ventricle (solid line) indicates how well each method performed.

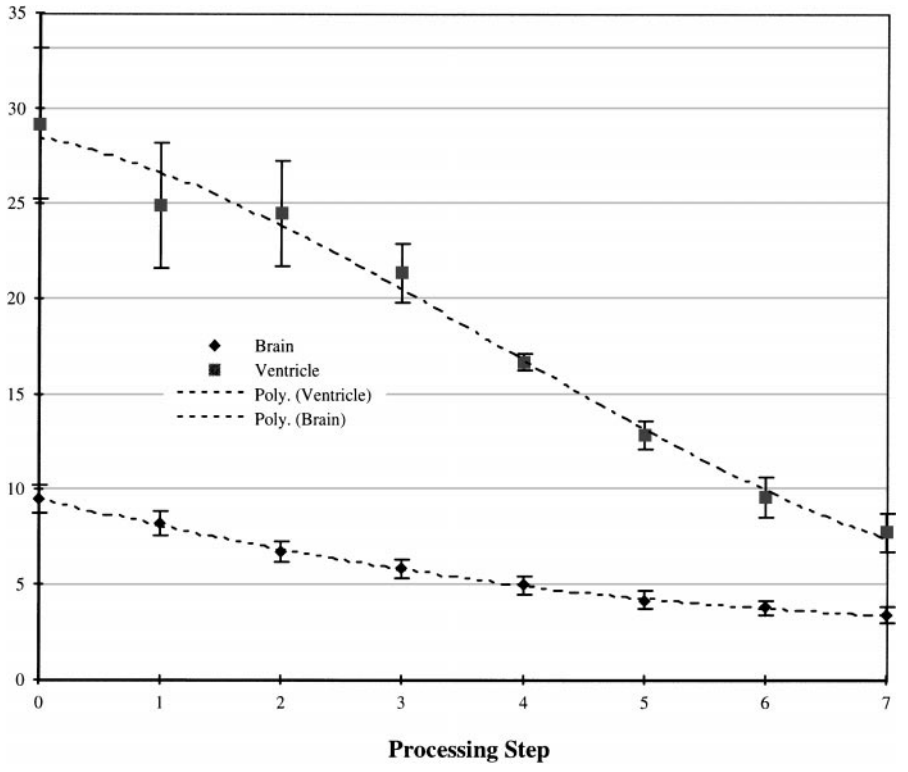

FIG. 9. Percentage boundary mismatch at each step of OSN processing for brain and lateral ventricle for fitting human brain images.

was not seen with human brain images. This is probably the result of numerous other structures within the human brain image that moderate the out-of-scale effect. The percentage mismatch at step 0 (following global spatial normalization) is similar to that measured using the homogeneous brain model (Fig. 7). However, the final mismatch for the human brain images is approximately 3% higher for brain and ventricle boundaries. These differences are probably due to the more complex (nonhomogeneous) nature of feature content for the human brain image, and interactions with feature matching that can occur.

The general trend in boundary mismatch was decreasing standard deviation for successive processing steps. This trend suggests a reduction in anatomical differences at boundaries of brain images from the different subjects. For the ventricle the lowest standard deviation was seen at step 4 (octant dimension = 16 mm). This may be due to small features near the ventricle border that confound the final fit. However, the mean percentage mismatch continued to improve down to step 7 (octant dimension = 2 mm) for both brain and ventricle surfaces. An important result of this test was that the boundary of the lateral ventricle was transformed independently of the brain boundary.

Processing time. Total image processing time for the OSN application, including loading source and target volumes, performing regional spatial normalization and saving the transformed image, is less than 10 min for a 256^3 3-D volume image (SUN Ultra 30–248 Mhz, SpecFP-95 11.4, Sun Microsystems, Mountain View, CA). A more detailed breakdown of processing speed for computer modeled cubes gave a total processing time of 8 min, with $3\frac{1}{2}$ min related to OSN fitting and $4\frac{1}{2}$ min for loading source/target images and saving the transformed image.

DISCUSSION

A fast method for 3-D spatial normalization of the human brain, called octree spatial normalization or OSN, was introduced. Its ability to generate continuous regional deformation was tested and demonstrated in several models. Global translation and scaling were carefully evaluated in solid models of cubes and spheres. A smooth, continuous transformation was seen even in the presence of gross nonhomology between source and target brain volumes. Regional independence was demonstrated for the surfaces of the brain and the lateral ventricle in a brain model. Preliminary results in human brain images yielded fit quality similar to that in the brain model.

Continuity correction. In current experiments the allowed maximum gradient magnitude was ≤ 0.3 to maintain the positivity of the determinant of the Jacobian matrix (Appendix 1). This was done for processing

steps 1 to 5, but continuity correction was not used in steps 6 and 7 since the octant dimensions were too small (4 and 2 mm). Also, large deformation field discontinuities, such as those used to demonstrate continuity problems in Figs. 1 and 3 (10 mm), were not present in human brain images, since global spatial normalization was performed prior to regional spatial normalization, and it corrects for most of the large-scale differences.

Global translation and scaling. Two-dimensional global translation, rotation, and scaling features of a 2-D version of the OSN method were previously reported (Lancaster *et al.,* 1998). Tests with simple elongated rectangles showed that global spatial normalization could be performed with a quadtree method. Tests indicated that while this was possible, it is more efficient to perform global spatial normalization with proven simpler transform methods, and this was done with 3-D processing of human data.

Scaling of the outer dimensions of the solid cube model was exact. For objects with outer boundaries definable as planes, the OSN processing appeared to perform perfectly. The scaling linearity within the cubes was also very good (Fig. 5). The ideal nature of the OSN boundary fit for cubes is believed to be related to the similarity of shape between octants used for processing and the cube shape. For example, in step 0 the source and target centroids are matched. At step 1, each octant contains a cubic region different only by size between source and target but with identical feature homology, i.e., cubic shape. For subsequent steps, this trend continues for octants near boundaries. Internal octants have identical centroids and no longer contribute to the deformation. No mismatched feature pairing was seen (source and target octants not full or partial cubes). This led to the near-perfect global linear scaling for each component of the deformation field, and when used with N-N interpolation the small differences fell near to the correct faces, resulting in a perfect fit at the boundary.

The solid sphere model presented a greater challenge since it did not subdivide into cubic suboctant features. However, the stepwise progress of processing (Fig. 4) shows that OSN algorithm performed well. The ability of the OSN algorithm to produce a smooth transformation, even when large discontinuities are present, is reemphasized here. By design, the step-1 local discontinuities were as high as 20 mm/voxel since global spatial normalization was not used in step 0. However, the surface appears relatively smooth and the shape is minimally distorted in early stages of processing. After step 3, volume differences are minimal, but small variations from the spherical shape remain. After step 7 the spheres are almost identical. Residual differences were partly attributed to the N-N interpolation.

Matching of nonhomologous regions. The goal of OSN for regions with nonhomologous features was to have a predictable, well-behaved transform with minimal effect on fit quality in regions where homologous features are present. Well behaved means no spatial discontinuities in transformed images, ensuring that the full source volume will be present in the transformed image.

Prior to continuity correction, it is important to minimize fluctuations in the uncorrected deformation field that might arise from mismatched features. Fluctuations were moderated by OSN's octant feature matching algorithm (Materials and Methods). The first step in this algorithm is to determine whether the set of voxels in the value min- to mid-range is larger than the set in the mid- to max-range, where mid = (max − min)/2. The geometric centroid of the larger set is calculated as the feature to match for each octant. Using a subset of the octant's voxels better concentrates feature analysis on the data within the octant, deemphasizing the boundary. It is also an attempt to isolate a *large* data region within the octant, similar to step 0 where the brain is fully contained within a single 256^3 region. When the step n source and target octants indicated different thresholding sense, feature mismatch was assumed, and the thresholding sense of the target used in both. This algorithm works well when features always match (i.e., 3-D solid cubes) and moderates the deformation in cases of nonhomologous features.

A modification of the OSN feature matching algorithm accounts for the case when either the source or target octant, but not both, are void of data. When this occurs, octants are enlarged by 50% until data are present in both. This mismatch can happen, even with homogeneous geometric models and is affected by the position of target and size differences between source and target. This feature was invoked during the fitting of the spherical computer models and worked very well (Figs. 4 and 5). When no data is present in a step n source and target octant no processing is done.

Regional performance. While several high-degree-of-freedom deformation methods have been developed, none has been able to resolve all regional differences. The good match for brain and ventricle in the brain model images indicates that OSN's regional deformation works well in this high-contrast model (Fig. 6). The slope of the percentage brain surface mismatch curve (Fig. 7) was steepest between step 0 and step 1, gradually decreased, but continued to be significant and negative through the last step. Interestingly, the fractional improvement increased with each step, with the largest percentage improvement between step 6 and step 7.

As mentioned in the results section, the positive slope in the percent surface mismatch for the modeled ventricle was probably due to an out-of-scale phenom-

enon. In fact, the slope did not become negative until step 3. The fit improvement at step 3 is assumed to be the result of a better match between octant dimension (32 mm) and the size of the lateral ventricle. The slope was more negative for each subsequent processing step, and this appears to compensate in part for the early processing. The desired fit quality was a percent mismatch below 1%, but only 5% mismatch was achieved for the ventricle. The final mismatch is, of course, dependent on structural homology between source and target ventricles, and this is the ultimate limiting factor. The final percentage boundary mismatch data indicate that brain surfaces are more homologous than ventricle surfaces, but this was expected since highly variable sulcal regions (Ono *et al.,* 1990) were excluded from the brain surface in this study.

Human brain evaluation. In the computer brain model the brain and ventricle were noiseless homogeneous regions surrounded by zero values. The human brain images differed from the brain model in that brain data were present in the space between ventricle and brain surfaces (Fig. 8). Outside the brain was set to zero and inside the ventricle was a single value equal to the average ventricle value. While the homogeneous ventricle did not mimic the ultimate use of OSN, it supports accurate measurement of percent mismatch for both the brain and ventricle in the human brain image. It also insures that internal differences between ventricles do not affect fit quality measurements. By using N-N interpolation the boundary for homogeneous areas around the brain and within the ventricle can be automatically tracked at each step of processing using simple thresholding.

The OSN feature-matching algorithm was developed for use with binary images (models) as well as gray-scale images. The algorithm uses the gray-scale image values to select the largest subset of voxels above or below the mid value for an octant. This serves to remove the influence of high or low values from the estimation of the feature centroid and render the data as binary (low value or high value set). Centroids calculated in this manner appear to better represent the *size* and *position* for the feature of interest within octants (Lancaster *et al.,* 1998). This helps to minimize the effect of differences in contrast between source and target images that are common in high-resolution 3-D MR images. By adapting to local values OSN is less affected by MR shading artifacts, and corrections for such are probably not necessary, though this has not been carefully tested.

Applications of the OSN algorithm. Two immediate applications of OSN are obvious. The first is to supplement the work of ANIMAL (Collins *et al.,* 1995) in the development of probability structures for the human brain (Mazziotta *et al.,* 1995). While ANIMAL provides a good method to create structure probability anatomical maps (SP_AMs), its processing time is long, delaying processing of large quantities of high-resolution images (approximately 33 h per image at full resolution). The processing time using OSN software is less than 10 min per brain volume, and it can be used on many different computer platforms since it was coded in *C++* with no graphical interface. While it is believed that OSN can perform this task well, a comparison between OSN and ANIMAL for generating SP_AMs must be performed before using it for this purpose.

The second intended use of OSN is to apply its deformations to functional images in an attempt to minimize regional anatomical variability. Functional images, coregistered to high-resolution MR images, will be transformed using the deformation field determined from the MR image. This testing will be done with PET images rather than fMRI since regional spatial distortions are minimal in PET. The goal is to improve multisubject functional studies by reducing the anatomical differences to a minimum before combining images from different subjects to create statistical probability images (SPIs) contrasting various tasks. Such processing could provide a basis to study correlation between spatial and functional variability. A key issue is whether regional spatial normalization will improve alignment of functional sites across subjects. If so, an increase in the signal-to-noise ratio in functional images beyond that seen for global spatial normalization would be expected, and the sensitivity of population studies improved. If the outcome is positive, and since OSN is ideally suited for cross-platform use, it could become a standard processing strategy for functional studies.

Other new applications. One potential application for OSN is to reregister images of body regions that deform plastically. This could be used, for example, in radiation treatment planning for organs such as the liver. OSN could be used to register CT or MRI images acquired with different body configurations and therefore deformed differently. These would be registered to the reference treatment volume defined using a 3-D CT simulator image. Another application would be to analyze the deformation fields to study regional growth patterns (i.e., plastic deformations) in 3-D (Toga *et al.,* 1998). For example, this would be useful to characterize regional tumor growth or shrinkage following treatment. Another potential application is the analysis of regional growth patterns in fossilized bones using CT images of ^{14}C-dated bone specimens. Deformation fields created using sequentially dated specimens can be used to describe spatial changes, and this should be helpful in the study of regional bone development on an evolutionary time scale.

Processing speed. A unique feature of the OSN algorithm is that it takes approximately the same time for each processing step, approximately 30 s. This is a

significant improvement over other hierarchical multiresolution methods where processing time increases significantly with each additional step (Collins *et al.,* 1995). Though the processing overhead increases slightly with each step for OSN, the number of void octants (no processing required) also increases, with the net effect of a slight drop in time/step toward later steps. The processing time is proportional to the number of voxels and for 128^3 images is approximately $\frac{1}{8}$ that for 256^3 images.

The preprocessing time for MRI brain images is longer than the OSN processing time. It takes 10–20 min to prepare a brain-only image. This is currently done using the MEDx (Sensor Systems, VA) interactive segmentation tools with touch up (if needed) using the Alice (Parexel Inc.) shrinkwrap and ROI nudging tools. Additionally, the brain image must be globally spatially normalized. This is done using the Convex Hull software (Lancaster *et al.,* 1999) and can be completed in approximately 5 min.

Algorithm problems. The OSN algorithm requires that all images have the same dimensions with 2^n size. In fact, it has only been tested for cubic voxels with 1 mm spacing in a 128^3 or 256^3 arrays. This is not considered to be a significant problem with the large amount of memory available for most computer systems.

In order to guarantee fit quality OSN processing must go through all steps. This is easily seen with the computer modeled sphere (Fig. 4). It is also indicated by the significant and continuous drop in mismatch error through the final step of processing (Figs. 7 and 9). This is not considered to be a significant problem since each processing step takes only 30 s.

Future developments. It is expected that the OSN algorithm will work well throughout the brain, but that has not been yet evaluated. Before proceeding with a more comprehensive evaluation throughout the brain, the low contrast capabilities of OSN will be enhanced and tested. The current feature matching strategy in OSN worked well with the high-contrast borders of solid models, a brain model, and several human brains. The matching of low-contrast structures presents a more difficult task; however, it is felt that with minimal modification of the feature matching algorithm this difficulty will be resolved. High speed cross-correlation between target and source octants is currently under review as a potential enhancement of the feature matching strategy.

Continuity correction will be extended to the final two processing steps (6 and 7) in the smaller octants ($4 \times 4 \times 4$ mm and $2 \times 2 \times 2$ mm). One proposal is to apply a small extent global filter throughout the entire volume with filter FWHM fixed for each size. Preliminary testing is underway, but it was not used in this evaluation of basic features of OSN.

Trilinear interpolation was incorporated into OSN with slight increase in processing time (3.5 to 5 min). It will be used in subsequent testing of the gray level matching ability of OSN throughout the brain. More accurate interpolation schemes, such as sinc interpolation (Hajnal *et al.,* 1995; Castleman, 1996) may eventually be used for the final reconstruction of transformed images. Multiple passes of the OSN algorithm over the source data, interpolated with higher order interpolation, is expected to improve mismatch of finer details. Although this may lead to the increase in the processing time, this has not yet been tested.

The use of OSN with other imaging modalities will rely on coregistration of those images with high-resolution MR images. The deformation will then be applied to the coregistered image. The overall performance of such multi-stage processing will need to be tested for the various methods in current use for registration (Pelizzari *et al.,* 1989; Woods *et al.,* 1992, 1993; Studholme *et al.,* 1995).

APPENDIX 1

Unique corrections were made to OSN's deformation field in an attempt to provide a piecewise continuous 3-D deformation with 1-to-1 mapping between source and target brain volumes. A coordinate transformation is locally 1-to-1 for 3-D images if the determinant of its Jacobian matrix is positive (Christensen *et al.,* 1995; Buck, 1978). OSN's deformation field is a set of vector equations like A.1, one for each *x-y-z* coordinate in the working volume.

$$\begin{bmatrix} x' \\ y' \\ z' \end{bmatrix} = \begin{bmatrix} x \\ y \\ z \end{bmatrix} + \begin{bmatrix} D_x(x, y, z) \\ D_y(x, y, z) \\ D_z(x, y, z) \end{bmatrix} \tag{A.1}$$

The determinant of the Jacobian for Eq. A.1 is calculated as follows

$$\begin{aligned} |\mathrm{J}| &= \begin{vmatrix} 1 + G_{xx} & G_{xy} & \mathrm{G}_{xz} \\ G_{yx} & 1 + G_{yy} & \mathrm{G}_{yz} \\ G_{zx} & \mathrm{G}_{zy} & 1 + G_{zz} \end{vmatrix} \\ |\mathrm{J}| &= 1 + (\mathrm{G}_{xx} + \mathrm{G}_{yy} + \mathrm{G}_{zz}) \\ &\quad + (\mathrm{G}_{xx}\mathrm{G}_{yy} + \mathrm{G}_{xx}\mathrm{G}_{zz} + \mathrm{G}_{yy}\mathrm{G}_{zz} \\ &\quad - \mathrm{G}_{xy}\mathrm{G}_{yx} - \mathrm{G}_{xz}\mathrm{G}_{zx} - \mathrm{G}_{yz}\mathrm{G}_{zy}) \\ &\quad + (\mathrm{G}_{xx}\mathrm{G}_{yy}\mathrm{G}_{zz} + \mathrm{G}_{xy}\mathrm{G}_{yz}\mathrm{G}_{zx} + \mathrm{G}_{xz}\mathrm{G}_{yx}\mathrm{G}_{zy} \\ &\quad - \mathrm{G}_{xx}\mathrm{G}_{yz}\mathrm{G}_{zy} - \mathrm{G}_{xz}\mathrm{G}_{yy}\mathrm{G}_{zx} - \mathrm{G}_{xy}\mathrm{G}_{yx}\mathrm{G}_{zz}) \end{aligned} \tag{A.2}$$

where the $G_{ij} = \Delta D_i/\Delta j$ $(i, j = x, y, z)$ are gradients of deformation field components.

For 3-D images the determinant of the Jacobian ($|J|$) is a measure of how differential volumes map between source and target regions. For global translation and rotation, there is no volume change ($|J| = 1$). The value of $|J|$ can increase or decrease depending on the nature of global scaling (expansion increases $|J|$ and contraction decreases $|J|$). $|J| < 0$ indicates a reflection of a volume through itself. These features are readily verified for a global affine coordinate transform. $|J| = 0$ indicates mapping of one or more points to a single point (loss of 1-to-1 nature) and poses a problem with higher order coordinate transformations, such as deformation fields, where both transform (A.1) and $|J|$ vary spatially. For OSN, spatial variations in $|J|$ are greatest at octant boundaries, so the continuity correction scheme was devised to constraint $|J|$ around octant boundaries. This constraint is applied to differential deformation fields before updating the full differential field.

The positivity of $|J|$ should be tested for each location in the volume of interest (i.e., the brain) to insure a continuous 1-to-1 transformation. Since this is extremely time consuming, $|J|$ was evaluated for what is believed to be the worst-case condition (isometric contraction), and a processing method developed to ensure that $|J| > 0$. During OSN processing, isometric contraction can occur for the eight voxels at the common boundary (vertex) of eight octants. This contraction was seen when warping cubes and spheres to smaller versions, following centroid matching. For isometric contraction $|J|$ reduces to

$$|J| = 1 + (G_{xx} + G_{yy} + G_{zz}) + (G_{xx}G_{yy} + G_{xx}G_{zz} + G_{yy}G_{zz}) + (G_{xx}G_{yy}G_{zz}), \quad \text{(A.3)}$$

where all G_{ii} are equal. Cancellation of cross-terms was verified by manual calculation. Equation A.3 predicts that $|J| = 0$ when $G_{ii} = -1$, $|J| < 0$ for $G_{ii} < -1$, and $|J| > 0$ for $G_{ii} > -1$. For the $|J| = 0$ case all eight voxels at the common vertex transform (contract) to the same location. When one or more voxels map to the same location, local failure of 1-to-1 mapping occurs. To avoid this condition we limited the magnitude of all G_{ij} at all octant boundaries to less than 0.3, a somewhat conservative restriction. To achieve this limit each differential deformation field component (D_x, D_y, and D_z) was smoothed using an adaptive 1-D Gaussian filter (See Fig. 3) across all eight octant faces.

The following steps illustrate calculation of the FWHM of the Gaussian filter for the D_x component of the deformation field along an x-directed line crossing between two octants:

1. The maximum value of G_{xx} before filtering is for points at the boundary between octants 1 and 2 (See dotted line in Fig. 3). At the boundary, $|G_{xx}| = |D_{x1} - D_{x2}|$, where D_{x1} and D_{x2} are the x-directed deformations for octants 1 and 2 before filtering. If $|G_{xx}|$ is < 0.3 no filtering is done.

2. The postfiltering maximum of G_{xx} is similarly calculated as $|G'_{xx}| = |D'_{x1} - D'_{x2}|$. The postfiltering deformations at octant boundaries are

$$D'_{x1} = \cdots + S_{-2}D_{x1} + S_{-1}D_{x1} + \mathbf{S_0D_{x1}} + S_{+1}D_{x2} + S_{+2}D_{x2} + \cdots$$

$$D'_{x2} = \cdots + S_{-2}D_{x1} + S_{-1}D_{x1} + \mathbf{S_0D_{x2}} + S_{+1}D_{x2} + S_{+2}D_{x2} + \cdots$$

where the Ss are the Gaussian weight factor for filtering at distances of 0, ± 1, ± 2, . . . voxels from the center of the filter. During subtraction all but bold terms cancel revealing a simple functional relationship among $|G'_{xx}|$, S_0, and $|G_{xx}|$

$$|G'_{xx}| = |D'_{x1} - D'_{x2}| = S_0\,|D_{x1} - D_{x2}| = S_0\,|G_{xx}| \quad \text{(A.4)}$$

3. For a Gaussian filter S_0 is defined as

$$S_0 = \frac{1}{\sqrt{2\pi\sigma}} = \frac{0.94}{FWHM} \quad \text{where } FWHM = 2.35\sigma. \quad \text{(A.5)}$$

4. Combining Eqs. (A.4) and (A.5) and setting the target maximum value of $|G'xx|$ to 0.3 leads to a simple equation for *FWHM* in terms of the prefiltering gradient magnitude

$$\mathbf{FWHM = 3.13\,|G_{xx}|} \quad \text{(A.6)}$$

For the example in Fig. 3, where G_{xx} was 10 at the boundary prior to filtering the *FWHM* used for filtering was 31.3 mm since voxel spacing was 1 mm.

ACKNOWLEDGMENTS

Research support was provided by the Human Brain Project, which is funded jointly by NIMH and NIDA (P20 MH/DA52176).

REFERENCES

Buck, R. 1978. *Advanced Calculus,* 3rd ed. McGraw-Hill, St. Louis, MO.

Castleman, K. 1996. *Digital Image Processing,* pp. 115–141. Prentice Hall, NJ.

Collins, D., Neelin, P., Peters, Y., and Evans, A. C. 1994. Automatic 3D intersubject registration of MR volumetric data in standardized space. *J. Comput. Assist. Tomogr.* **18:**192–205.

Collins, D., Holmes, C., Peters, T., and Evans, A. 1995. Automatic 3-D model-based neuroanatomical segmentation. *Hum. Brain Mapp.* **3**(3):190–208.

Christensen, G., Rabbitt, R., and Miller, M. 1994. 3D brain mapping using a deformable neuroanatomy. *Phys. Med. Biol.* **39:**609–618.

Christensen, G., Rabbitt, R., Miller, M., Joshi, S., Grenander, U., Coogan, T., and Van Essen, D. 1995. Topological properties of smooth anatomic maps. In *Information Processing in Medical Imaging: 14th International Conference* (Y. Bizais, C. Braillot, and R. Di Paola, Eds.), Vol. 3, pp. 101–112. Kluwer, MA.

Fox, P., Perlmutter, J., and Raichle, M. 1985. A stereotactic method of anatomical localization for positron emission tomography. *J. Comput. Assist. Tomogr.* **9:**141–153.

Fox, P. 1995. Spatial normalization origins: Objectives, applications, and alternatives. *Hum. Brain Mapp.* **3**(3):161–164.

Friston, K. J., Ashburner, J., Frith, C. D., Polint, J. B., Heather, J. D., and Frakowiak, R. S. J. 1995. Spatial registration and normalization of images. *Hum. Brain Mapp.* **3**(3):165–189.

Foley, J., van Dam, A., Feiner, S., and Hughes, J. 1990. *Computer Graphics Principles and Practice,* 2nd ed., Chap. 6. Addison-Wesley.

Hajnal, J., Saeed, N., Soar, E., Oatridge, A., Young, I., and Bydder, G. 1995. A registration and interpolation procedure for subvoxel matching of serially acquired MR images. *J. Comput. Assist. Tomogr.* **19**(2):289–296.

Hasegawa, B. H. 1991. *The Physics of Medical X-Ray Imaging,* Chap. 6. Medical Physics Publishing, Madison, WI.

Kostelec, P., Weaver, J., and Healy, D. 1998. Multiresolution elastic image registration. *Med. Phys.* **9**(25):1593–1604.

Lancaster, J. L., Glass, T. G., Lankipalli, B. R., Downs, H., Mayberg, H., and Fox, P. T. 1995. A modality-independent approach to spatial normalization of tomographic images of the human brain. *Hum. Brain Mapp.* **3**(3):209–223.

Lancaster, J. L., Rainey, L. H. T. G., Summerlin, J. L., Freitas, C. S., Fox, P. T., Evans, A. C., Toga, A. W., and Mazziotta, J. C. 1997. Automated labeling of the human brain: A preliminary report on the development and evaluation of a forward-transform method. *Hum. Brain Mapp.* **5**(5):238–242.

Lancaster, J. L., Kochunov, P. V., Fox, P. T., and Nickerson, D. 1998. k-Tree method for high-speed spatial normalization. *Hum. Brain Mapp.* **6:**358–363.

Lancaster, J., Fox, P., Downs, H., Nickerson, D., Hander, T., Mallah, M., and Zamarripa, F. 1999. Global spatial normalization of the human brain using convex hulls. *J. Nucl. Med.,* **40:**942–955.

Mazziotta, J. C., Toga, A. W., Evans, A., Fox, P., and Lancaster, J. 1995. A probabilistic atlas of the human brain: Theory and rationale for its development. *Neuroimage* **2:**89–101.

Minoshima, S., Koeppe, R. A., Mintum, M., Berger, K. L., Taylor, S. F., Frey, K. A., and Kuhl, D. E. 1993. Automated detection of the intercommissural line for stereotaxic localization of functional brain images. *J. Nucl. Med.* **34:**322–329.

Ono, M., Kubik, S., and Abernathey, C. 1990. *Atlas of the Cerebral Sulci.* Theime, NY.

Pelizzary, C., Chen, G., *et al.* 1989. Accurate three-dimensional of CT, PET, and/or MR images of the brain. *J. Comput. Assist. Tomogr.* **13**(1):20–26.

Pelizzary, C. 1991. *Installation and User's Guide for the University of Chicago Image Registration Software (XSurfaceFit).*

Roland, P. E., Graufelds, C. J., Wahlin, J., Ingleman, L., Andersson, M., Ledberg, A., Pederson, J., Akerman, S., Dabringhaus, A., and Zilles, K. 1994. Human brain atlas: For high-resolution functional and anatomical mapping. *Hum. Brain Mapp.* **1:**127–184.

Studholme, C., Hill, D., and Hawkes, D. 1995. Multiresolution voxel similarity measurements for MR-PET coregistration. In *Information Processing in Medical Imaging,* pp. 287–298.

Talairach, J., and Tournoux, P. 1988. *Co-Planar Stereotaxic Atlas of the Human Brain.* Thieme, New York.

Toga, A., and Thompson, P. 1988. An introduction to brain warping. In *Brain Warping,* pp. 1–26. Academic Press.

Woods, R., Cherry, S., *et al.* 1992. Rapid automated algorithm for aligning and reslicing PET images. *J. Comput. Assist. Tomogr.* **16**(4):620–633.

Woods, R., Mazziotta, J., *et al.* 1993. MRI-PET registration with automated algorithm. *J. Comput. Assist Tomogr.* **17**(4):536–546.

Woods, R. 1996. Correlation of brain structure and function. In *Brain Mapping the Methods* (A. Toga and J. Mazziotta, Eds.), pp.313–342. Academic Press.